IOPscience iopscience.iop.org

Home Search Collections Journals About Contact us My IOPscience

Morphological evolution of InAs/InP quantum wires through aberration-corrected scanning transmission electron microscopy

This article has been downloaded from IOPscience. Please scroll down to see the full text article.

2010 Nanotechnology 21 325706

(http://iopscience.iop.org/0957-4484/21/32/325706)

View the table of contents for this issue, or go to the journal homepage for more

Download details:
IP Address: 128.219.49.9
The article was downloaded on 14/02/2011 at 19:58

Please note that terms and conditions apply.

Nanotechnology **21** (2010) 325706 (8pp) doi:10.1088/0957-4484/21/32/325706

Morphological evolution of InAs/InP quantum wires through aberration-corrected scanning transmission electron microscopy

D L Sales[1], M Varela[2], S J Pennycook[2], P L Galindo[3], L González[4], Y González[4], D Fuster[5] and S I Molina[1]

[1] Departamento de Ciencia de los Materiales e I. M. y Q. I., Universidad de Cádiz, Campus Río San Pedro, E-11510 Puerto Real, Cádiz, Spain
[2] Materials Science and Technology Division, Oak Ridge National Laboratory, Oak Ridge, TN 37831, USA
[3] Departamento de Lenguajes y Sistemas Informáticos, Universidad de Cádiz, Campus Río San Pedro, E-11510 Puerto Real, Cádiz, Spain
[4] Instituto de Microelectrónica de Madrid (CNM, CSIC), Isaac Newton 8, E-28760 Tres Cantos, Madrid, Spain
[5] UMDO (Unidad Asociada al CSIC-IMM), Instituto de Ciencia de Materiales, Universidad de Valencia, PO Box 22085, 4607 Valencia, Spain

E-mail: david.sales@uca.es

Received 5 March 2010, in final form 21 June 2010
Published 21 July 2010
Online at stacks.iop.org/Nano/21/325706

Abstract
Evolution of the size, shape and composition of self-assembled InAs/InP quantum wires through the Stranski–Krastanov transition has been determined by aberration-corrected Z-contrast imaging. High resolution compositional maps of the wires in the initial, intermediate and final formation stages are presented. (001) is the main facet at their very initial stage of formation, which is gradually reduced in favour of {114} or {118}, ending with the formation of mature quantum wires with {114} facets. Significant changes in wire dimensions are measured when varying slightly the amount of InAs deposited. These results are used as input parameters to build three-dimensional models that allow calculation of the strain energy during the quantum wire formation process. The observed morphological evolution is explained in terms of the calculated elastic energy changes at the growth front. Regions of the wetting layer close to the nanostructure perimeters have higher strain energy, causing migration of As atoms towards the quantum wire terraces, where the structure is partially relaxed; the thickness of the wetting layer is reduced in these zones and the island height increases until the (001) facet is removed.

(Some figures in this article are in colour only in the electronic version)

1. Introduction

The growth of three-dimensional (3D) semiconductor nanostructures is achievable by several different approaches. Self-assembly, through the Stranski–Krastanov (SK) growth mode, is recognized as one of the most remarkable ones. This growth mode involves pseudomorphic (bidimensional) growth of a material on top of another one with high lattice misfit (larger than about 2%), so it spontaneously experiences a transition to 3D growth [1, 2]. This transition happens when the accumulated biaxial stress exceeds a given value, after a critical thickness is attained.

For the heteroepitaxial system InAs/InP, with a 3.2% misfit, this approach leads to the formation of quantum wires (QWRs) under certain conditions through molecular beam epitaxy (MBE) [3]. The InAs/InP system has attracted much interest because of its potential applications for telecommunication technologies. Several parameters

 © 2010 IOP Publishing Ltd Printed in the UK & the USA

make it possible to control their emission properties from 1.2 to 1.9 μm [4], such as the angle at which they stack when growing multiple layers [5, 6], or their density [7], offering the possibility of isolating quantum wires for their integration in new quantum information devices. Hence, a considerable effort has been devoted to learning about the nucleation and evolution of nanostructures grown by the SK mode. Nevertheless, the process of self-assembly for these nanostructures is not entirely understood yet, particularly across the critical SK transition.

This paper aims to characterize the morphological and compositional evolution of the QWRs from the initial formation stages and into the growth process. Size, shape and composition distribution of buried QWRs is measured with atomic column resolution, along with quantified compositional maps at sub-nanometre resolution. The observed changes of size and shape are explained in terms of strain energy variations along the growth front. Layer-by-layer compositional profiles can be extracted from aberration-corrected scanning transmission electron microscopy (STEM) Z-contrast images, giving experimental evidence of the role of the wetting layer in donating atoms into the island. A detailed picture of the Stranski–Krastanov growth mode is thereby obtained. Such Z-contrast images and electron energy loss (EEL) spectra provide spatial and energy resolutions near or below 1 Å and 0.5 eV, respectively, which offer dramatically improved resolution and sensitivity for determining atomic arrangements [8–10]. STEM measurements on InAsP QWRs coupled to elasticity calculations by finite element methods (FEM) have previously been used to explain their preferred nucleation site on single [11] and stacked layers [5].

Unlike atomic force microscopy (AFM), the present approach permits both buried and surface nanostructures to be analysed with high spatial resolution. This is especially important for a correct correlation between structural and optical properties, as buried (potentially emitting) nanostructures may differ from surface ones. Differences between uncapped and capped nanostructures may be due, on the one hand, to segregation and inter-mixing effects taking place during the growth of the capping layer and, on the other hand, to oxidation of surface layers when the sample is in contact with the air.

2. Characterization

2.1. Experimental set-up

2.1.1. Sample growth. This paper focuses on the analysis of three samples, S23, S25 and S27, grown by solid source MBE, consisting of the growth of 2.3, 2.5 and 2.7 InAs monolayers (ML), in that order, on InP(001) at 0.5 ML per second (ML s^{-1}), substrate temperature of 480 °C and As_4 beam equivalent pressure of 640 Pa. Sample S25 corresponds to the onset of the elastic relaxation process due to the spontaneous self-assembling of QWRs, as measured by *in situ* measurements of accumulated stress during InAs deposition [7]. Accordingly, S23 and S27 correspond to situations just before (flat surface) and after (well-developed QWRs) the one of S25. Because of this rapid change in stress across the SK transition, it is possible to control the deposition very accurately and repeatably, to an estimated 0.05 ML. After the InAs deposition, the sample is annealed at a constant As_4 pressure for 90 s, and a 20 nm thick InP layer is grown to allow optical measurements. Then, the growth of the InAs layer is repeated for surface characterization using the same conditions. More growth details together with AFM images of superficial QWRs can be found in [7].

2.1.2. Electron microscopy. Cross-sectional specimens for STEM were produced by mechanical thinning and ion milling. A precision ion polishing system (PIPS) was used up to 3.5 kV and 4° of beam tilt until electron transparency. Z-contrast images and core loss EEL spectra have been acquired at 100 kV using a dedicated VG Microscopes HB501UX STEM with a Nion aberration corrector and a Gatan Enfina EEL spectrometer. EEL spectrum images were acquired with energies between the zero-loss peak and 1430 eV. The C signal was relatively low, showing very little contamination. The P L edge (132 eV) was used for quantification purposes. Elemental maps of P were obtained by first performing a background subtraction (power-law fit) using a window between 106 and 126 eV, then integrating the P signal between 127 and 137 eV and dividing it by the integrated background between 116 and 126 eV. In some sense, this is equivalent to the three-window technique widely used in energy-filtered transmission electron microscopy (EFTEM). Thickness maps (t/λ) showed that the specimen thickness in the area was very homogeneous and around 0.4 inelastic mean free paths.

2.2. STEM results

2.2.1. Size, shape and density of QWRs. The surface and the buried InAs layers have been analysed along the transparent area of the three samples. Low magnification Z-contrast images of these areas for the different samples are shown in figures 1(a), (d) and (g).

No QWRs were found in the sample with the smallest amount of deposited InAs, S23. A homogeneous InAs(P) wetting layer can be seen in its underlayer (figure 1(c)), but not in the surface (figure 1(b)), where an amorphous layer of 1.5 nm average thickness is observed instead. Oxidation is believed to occur at III–V semiconductor surfaces [12], which would be sufficient to explain the observed amorphous layer. This oxide layer does not allow accurate morphological measurements in superficial nanostructures.

Sample S25 corresponds to the earlier growth stage where the formation of nanowires occurs, with a linear density of 2.3×10^{10} cm^{-1}. Capped QWRs at this stage (figure 1(f)) are 1.5 nm high and 14.1 ± 0.6 nm wide, taking an average of 2 QWRs. Figure 1(e) depicts a superficial QWR where just 3 ML (~0.9 nm) of InAs can be distinguished, with ~1 nm of oxide layer. A considerable reduction of the average dimension is observed in the uncapped (oxidized) QWRs compared to the capped ones.

The linear density of nanowires measured in sample S27, in which an increment of only 0.2 ML of deposited InAs takes place with respect to sample S25, increases up to 33.9×10^{10} cm^{-1}. Several buried and surface QWRs can be found in

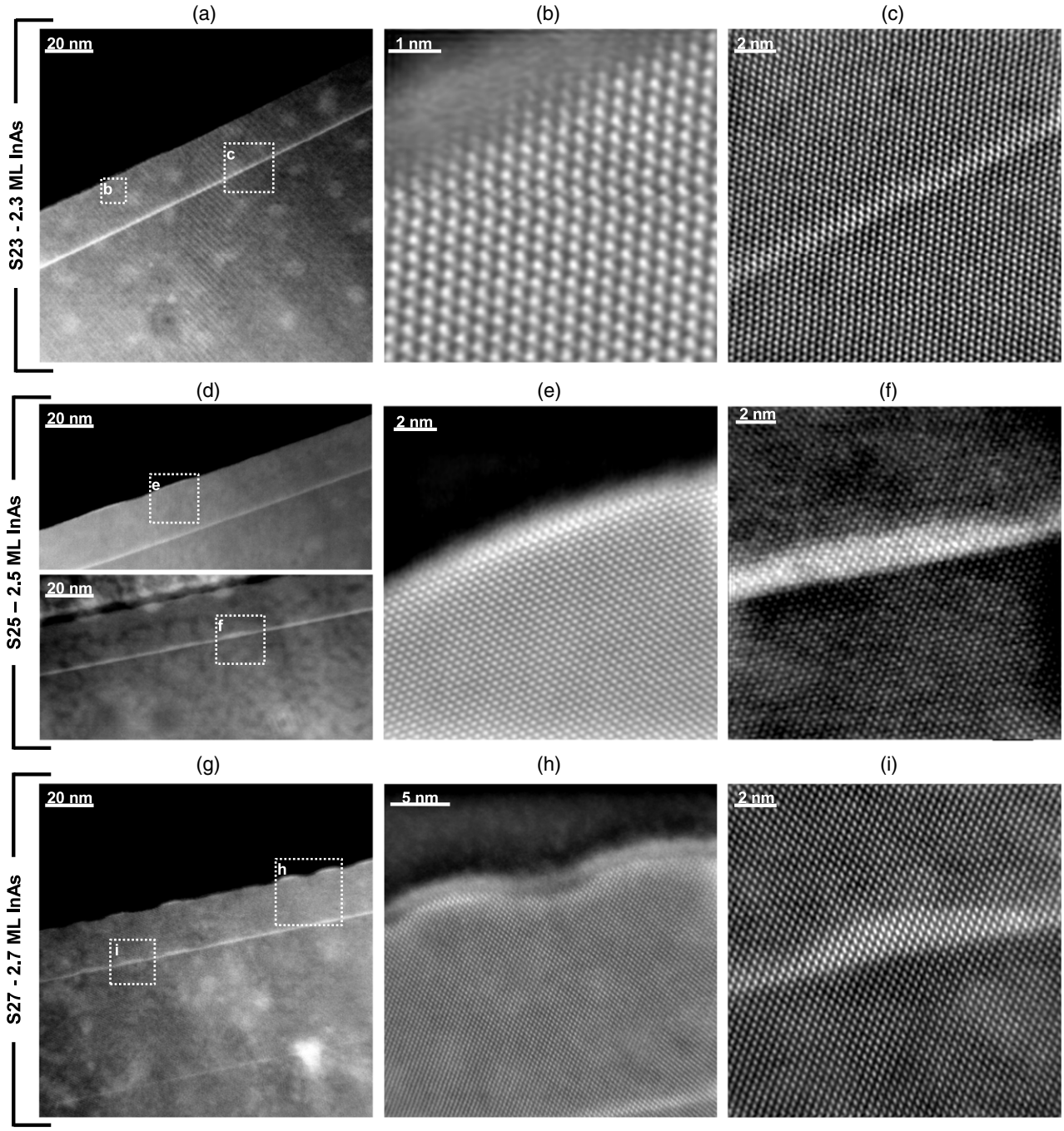

Figure 1. Z-contrast images of samples S23 ((a)–(c)), S25 ((d)–(f)) and S27 ((g)–(i)). High resolution images of surface ((b), (e), (h)) and buried InAs layers ((c), (f), (i)). Images have been low-pass-filtered for noise reduction.

figure 1(g). The average dimensions for the buried wires in this sample are 2.3 ± 0.3 nm height and 11.8 ± 1.0 nm width, and 1.4 ± 0.3 nm height and 10.6 ± 1.4 nm width for the uncapped ones, from measurements of four capped and five uncapped QWRs. This means an increase in height of $55 \pm 19\%$ and a reduction in width of $17 \pm 11\%$ in buried QWRs of sample S27 with respect to S25.

2.2.2. Composition. Chemical information can be extracted qualitatively from Z-contrast images to assess the As content in QWRs [13]. Figures 2(a) and (b) represent maps of the integrated intensity around As–P columns from high resolution Z-contrast images of samples S25 and S27. Integration areas have been taken to obtain significant signal-to-noise ratios. Higher values of integrated intensity denote higher As content. The resultant maps show a gradient of As content, with maximum concentration in the inner part of the QWR. Quantitative EELS analysis performed on a QWR of sample S27 (figure 2(c)) corroborates the chemical distribution and gives a minimum P content around zero, i.e. pure InAs, in the central zone of the nanowire shown in figure 2(d). This higher As content is consistent with the interpretation of the

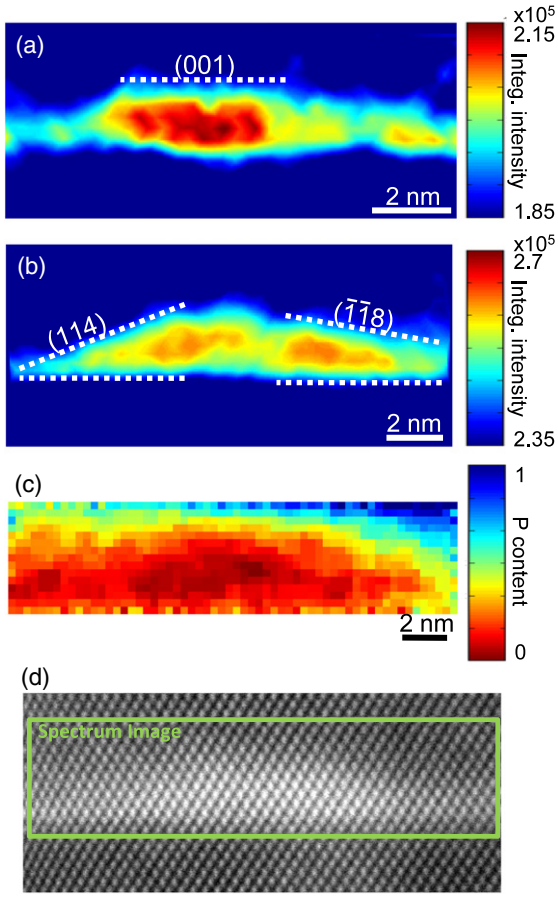

Figure 2. Maps of integrated intensities around As–P columns, measured from high resolution Z-contrast images of samples S25 (a) and S27 (b). Deep blue colour corresponds to InP. Main facets are highlighted with dotted lines. (c) P map quantified from EELS spectrum image of a QWR from sample S27. Pure InAs is found in the core. The area used for the spectrum image is highlighted in green in the HAADF image (d).

photoluminescence of these samples [14]. An asymmetrical As distribution is also appreciable in QWRs from their initial stages of growth. This asymmetry was already observed in mature wires as a consequence of strain asymmetry in superficial steps [11] and shown to be responsible for the tilt angle of QWRs in stacked layers [5, 6].

2.2.3. Faceting evolution. As we move from samples S25 to S27, a change in faceting is also appreciable from both the high resolution Z-contrast pictures and As/P intensity maps. Facet angles can be easily measured in the coloured maps of figures 2(a) and (b). This evolution is shown schematically in figure 3: (001) facets are predominant at the most initial stage (sample S25, figure 1(f)), while they are replaced by {114} (mainly) and {118} facets as the growth proceeds (sample S27, figure 1(i)). Images of mature QWRs with similar growth process (e.g. figure 2 in Molina *et al* [11]) showed {114} as the most stable facets. This faceting evolution observed in buried structures is in agreement with the RHEED analysis of the growth surface reported by Gutiérrez *et al* [15] for a similar system, proving that these facets are preserved after growth of the upper confining layer.

Table 1. Summary of size and linear density measurements on initial QWRs from aberration-corrected Z-contrast images. Statistical dispersion is included.

InAs deposited (ML)	Width (nm)	Height (nm)	Linear density (cm^{-1})
2.5	14.1 ± 0.6	1.5 ± 0.0	2.3×10^{10}
2.7	11.8 ± 1.0	2.3 ± 0.3	33.9×10^{10}

3. Simulation

To understand this morphological evolution, simulations of the elastic energy on the growth front surface have been carried out, solving the anisotropic elastic theory equations by FEM.

3.1. The model

The STEM-EELS characterization allows the building of an accurate structural model. This model can then be used as input for simulations of the variation of elastic energy as a function of the QWR growth process. Two models were defined, corresponding to the situation of samples S25 and S27. Size, shape, composition, boundary conditions and elastic parameters of the materials were taken into account.

3.1.1. Size and shape. The size and shape of the wire structures have been modelled on the basis of Z-contrast high resolution images of buried nanostructures, with enough sensitivity to define those aspects with atomic column resolution. Measurements of uncapped superficial wires were not considered, due to their significant oxidation. The thickness of the wetting layer in the model corresponds to the height of the total amount of deposited InAs minus the amount used to form the QWRs. The observed QWR linear density in table 1 has been taken into account for this calculation.

3.1.2. Composition. Pure InP is considered for the substrate and pure InAs for the wetting layer and quantum wires.

3.1.3. Boundary conditions. Three-dimensional quantum wires are modelled and symmetries are then incorporated into the calculations to represent the entire sample. The periodicity of the structure is chosen considering the observed QWR linear density and it is taken into account by applying the appropriate boundary conditions: all the nodes of symmetry planes are fixed against displacement in the directions normal to these planes, and all nodes on the bottom of the substrate are fixed against rigid body shift in the z direction.

3.1.4. Elastic parameters. Anisotropic behaviour and values at 300 K are assumed for elastic constants. Properties of InAs and InP have been taken from [16], summarized in table 2.

3.2. Calculations

In order to introduce the stress induced by the lattice mismatch between the epilayer and the substrate, an initial strain condition needs to be applied. In this sense, we proceed as in

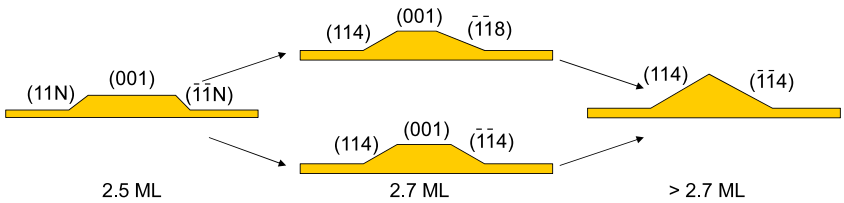

Figure 3. Example scheme of the observed shape evolution of InAs(P) self-assembled quantum wires.

Table 2. Lattice constants and anisotropic material properties of InP and InAs.

Material	a (nm)	c_{11} (GPa)	c_{12} (GPa)	c_{44} (GPa)
InP	5.8687	101	56.1	45.6
InAs	6.0583	83.4	45.4	39.5

the commonly accepted procedure [17, 18] where the deposited material (InAs in our case) is strained an amount equal to the lattice misfit, $f(1)$. This means a compressive strain of 3.2% for pure InAs on InP in the three perpendicular directions (x, y and z, corresponding to crystal orientations [110], [1$\bar{1}$0] and [001], respectively), $\varepsilon_1 = \varepsilon_2 = \varepsilon_3 = -0.032$ being the initial conditions, where ε_1, ε_2 and ε_3 represent the three diagonal components of the strain tensor:

$$f = \frac{a_{\mathrm{InAs}} - a_{\mathrm{InP}}}{a_{\mathrm{InP}}}. \tag{1}$$

Once the initial strain condition is assigned, the system evolves up to a final relaxed state solving by FEM Hooke's law for the anisotropic elasticity theory, shown in (2) in matrix notation, where σ_i, C_{ij} and ε_j are the stress, stiffness (elastic coefficients) and strain tensors, respectively. This is done by the commercial FEM solver *Comsol Multiphysics* code. At the end of the calculation, the continuum elastic body satisfies the null-stress condition $\sigma \cdot n = 0$, where n is the normal to any free surface:

$$\sigma_i = C_{ij} \cdot \varepsilon_j. \tag{2}$$

3.3. Results

The results from this calculation are shown in figure 4, where in-plane strain (ε_{xx}) and strain in the growth direction (ε_{zz}) are plotted in coloured maps on the 3D models representing the nanowires. Figure 4(a) shows how strain at the sides of the QWR results in a larger in-plane lattice parameter with respect to the wetting layer area. This would mean easier InAs (higher lattice parameter than InP) incorporation in these areas. In contrast, the border of the QWR with the wetting layer shows a reduction of the in-plane lattice parameter with respect to relaxed InP. Those areas of the surface where the in-plane lattice parameter is smaller (where InAs would grow highly compressed) present a larger chemical potential and therefore less probability of further InAs deposition, and hence more superficial diffusion of As outwards. Positive strain along the [001] direction (i.e. growth direction) is always found in the InAs layer (figure 4(b)), due to the tetragonal distortion caused by the in-plane compressive misfit of InAs with respect to the InP substrate. This strain is less noticeable in the QWRs than in the wetting layer because their 3D shape provides the opportunity to relax parallel to the heterointerfaces (see details within the circles of figure 4).

Although strain maps might help us to get a picture of the growth front surface, it is more convenient to analyse this surface in terms of energy or chemical potential. An analysis of the chemical potential on the growth front surface would allow understanding its morphological evolution, identifying the low energy regions as preferential bounding sites for free atoms in the MBE growth chamber or for adatoms diffusing across the surface. The chemical potential μ can be estimated as a sum of contributions $\mu = \mu_0 + \mu_{\mathrm{E}} + \mu_{\mathrm{S}} + \mu_{\mathrm{M}}$, where μ_0 is the chemical potential of a flat and unstressed surface, μ_{E} takes into account the elastic energy stored in the material, μ_{S} evaluates the influence of the surface energy and therefore depends on the surface curvature [19] and μ_{M} is the chemical potential related to the entropy of mixing of the formed alloy [20]. In our case, μ_{M} can be considered to be independent on the surface site because the whole surface consists of the binary compound InAs. Therefore, the major contributors to the chemical potential are μ_{E} and μ_{S}. The term μ_{E} minimizes where the strain energy is minimum and μ_{S} minimizes in concave surface regions, favouring deposition at valleys [21].

Profiles of simulated strain energy (which is the energy stored in the material due to its strain) along [110] on the surface of QWRs of samples S25 (a) and S27 (b) are drawn in figure 5. The profiles obtained from both models show that the QWR (001) facets present lower strain energy than any other part on the surface. Additionally, higher strain energy values are placed in the joint between the WL and the QWR. Therefore, when the strain energy is the main contributor to the chemical potential, (001) facets will be the sites for preferential growth, leading to increasing the QWR height and defining the {114} (mainly) and {118} lateral facets. Therefore, the (001) facet is being reduced along the growth, until it disappears when the lateral facets become fully developed, as observed.

Surface diffusion is driven by variations of the chemical potential, resulting in atom migration from higher to lower chemical potential zones [22, 23]. Consequently, according to our model a net surface current is generated, biasing the atom motion on the surface preferentially towards the upper part of QWRs and away from their perimeters to nucleate other wires (see arrows in figure 5). Therefore, the evolution of the morphology of this system can be understood in terms of the elastic energy, the contribution of the surface energy term being negligible (μ_{S}) for the qualitative assessment of

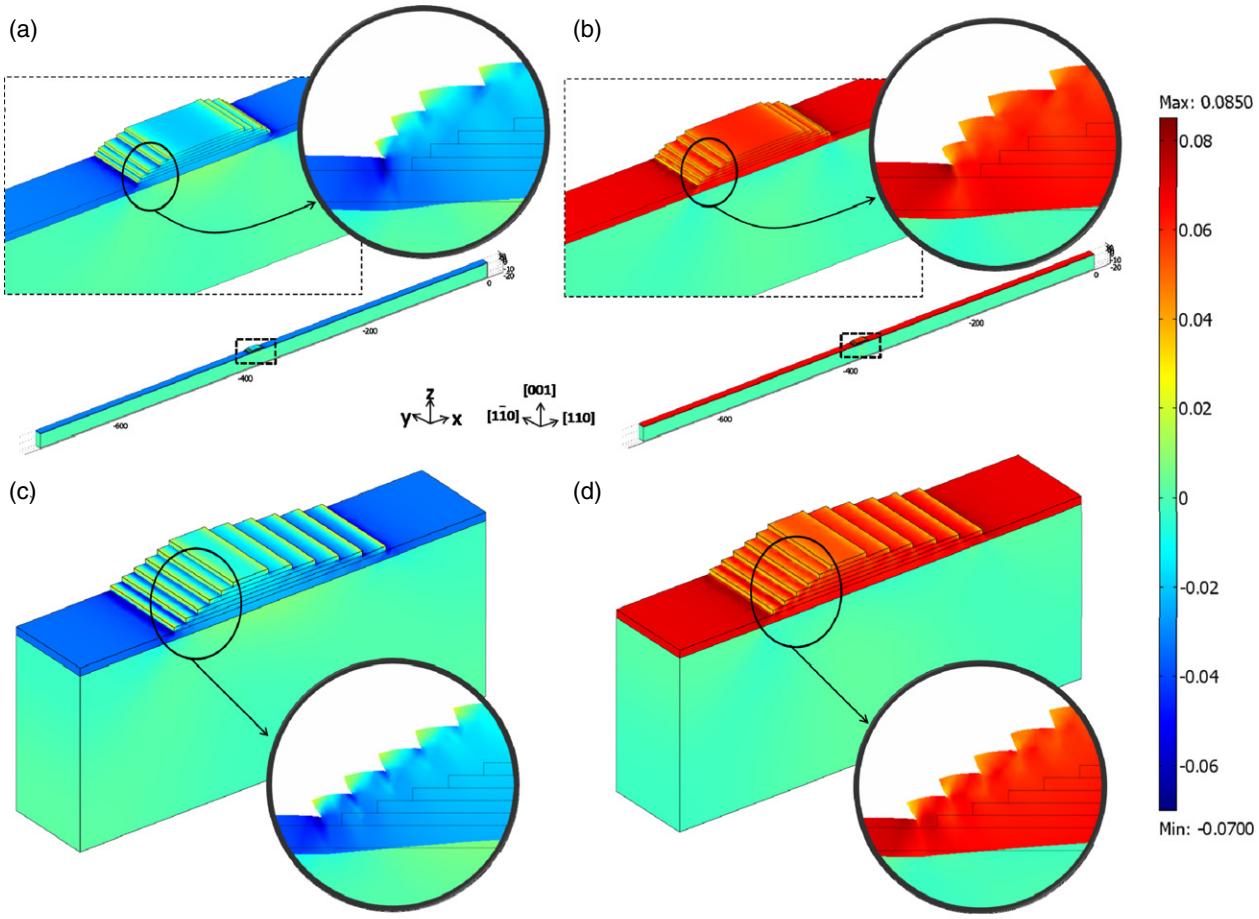

Figure 4. Simulated strain in the growth direction ((c) and (d)) and the in-plane direction ((a) and (b)) of initial QWRs corresponding to samples S25 ((a) and (b)) and S27 ((c) and (d)). Details of the deformed shape multiplied by a factor of 10 are also shown in circles.

the chemical potential. Nevertheless, more complex models, such as density functional theory (DFT) [24] or kinetic Monte Carlo (KMC) [25], need to be considered to get a more realistic scenario, but they are still limited for large structures. These results are consistent with calculations using analytical methods which describe the island self-assembling process [23, 26] and with other experimental evidence like that described by Cho *et al* for elongated islands [27]. One of the conclusions from our model is the active role of the wetting layer in the self-assembling process, as it is the main atom donor for the growth of nanostructures. Therefore, it is expected for the wetting layer to reduce its thickness during the growth, especially in the vicinity of the QWRs. This thickness reduction ends up with a change in the composition profile after the growth of the InP capping layer needed for photonics applications.

In order to corroborate this statement, the chemical profile of the wetting layer has been measured using the quantitative HAADF method mentioned in section 2.2.2. Figure 6 shows the As profile along [001] across the wetting layer of samples S23, S25 and S27, with an inset of one of the images used for quantification. The sample with the lowest amount of InAs (S23) does not register any QWR, while the others have the lineal density given in table 1. Due to the high density of wires in S27, the analysed HAADF image corresponds to an area in between two nearby QWRs. The wetting layers of samples S23 and S25 have high As concentrations, being close to pure InAs within the first three monolayers, and then decreasing as described by the standard segregation models [28]. However, the As concentration has been substantially reduced in sample S27.

These measurements explain the observed morphological evolution of the QWRs. The areas of the wetting layer close to the nanostructures have higher strain energy, resulting in the migration of As atoms towards the QWR terraces, where the lattice is partially relaxed. The thickness of the wetting layer is reduced in these zones, leading to a decrease of the As concentration after the wetting layer has been covered with the InP confining layer. This observation is consistent with the reproduction of the epitaxial island evolution shown by Tu and Tersoff for the Si/Ge system [29] and experimentally observed by Denker *et al* [30].

4. Conclusions

In summary, based on direct imaging by aberration-corrected STEM we have shown that self-assembled InAs/InP nanowires

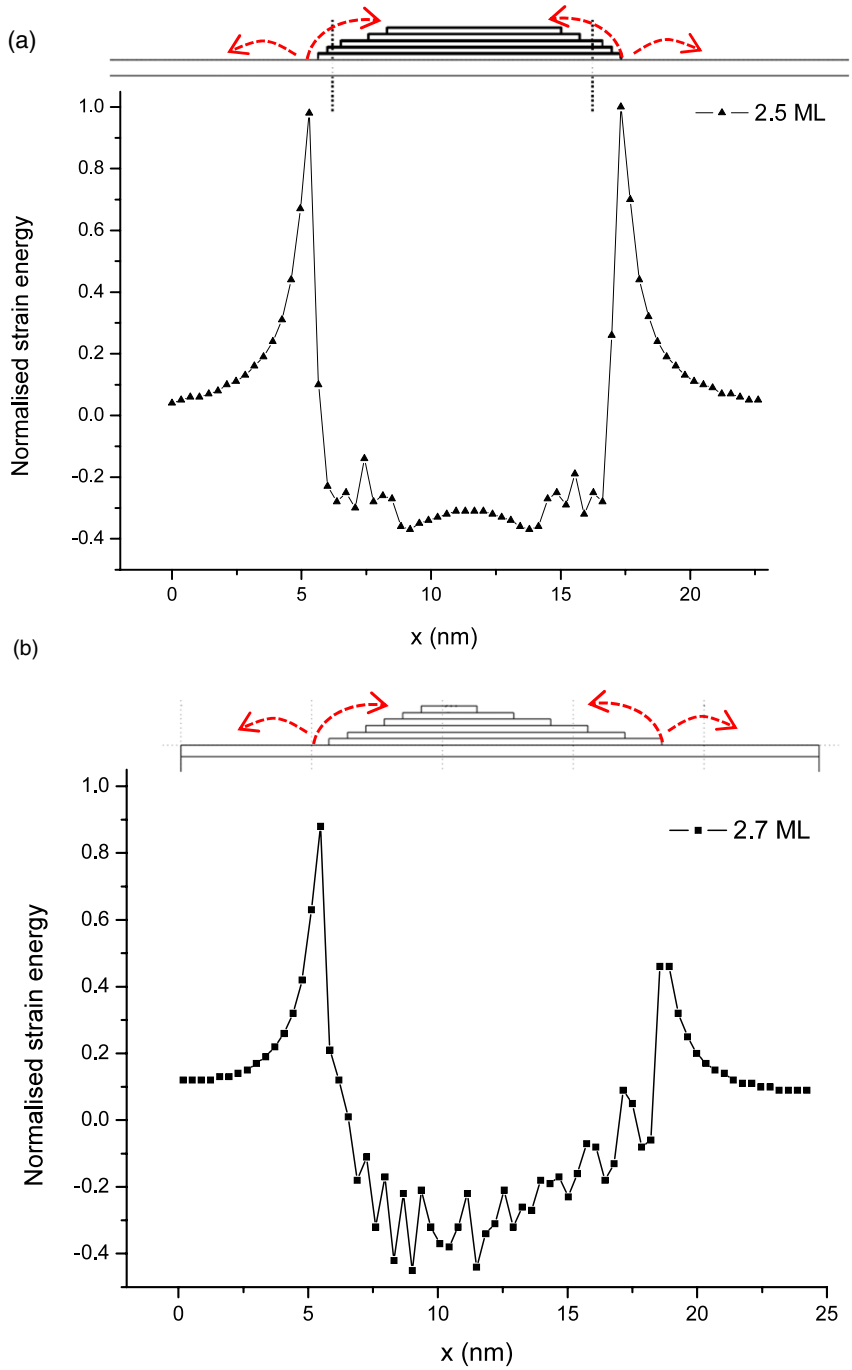

Figure 5. Simulated strain energy profiles along [110] on the surface of initial QWRs of samples S25 (a) and S27 (b). Strain energy is normalized with respect to the maximum registered value of both models. Cross sections of the QWR models are shown on top of the profiles to visualize the location of the strain energy values. Maxima are found in the joint between the WL and the QWR, while (001) facets present lower strain energy than any other part on the surface. Arrows indicate preferred directions for surface atom flux during growth.

evolve during their formation in such a way that (001) is the main facet in the initial stages of growth, which gradually becomes replaced by {114} and {118} facets, ending with the formation of mature QWRs with {114} facets. During this evolution process, the height of the QWRs increases, on average, up to 55%, whereas their width reduces by as much as 17%. These significant morphological changes occur on increasing the amount of deposited InAs by only 0.2 ML. The arsenic distribution in the QWRs is asymmetric from their initial stage of formation, presenting a highly concentrated core. Subsequent morphological evolution is explained in terms of variation of the elastic energy at the growth front of InAs/InP initial QWRs, calculated by FEM models. These calculations locate energy minima on (001) facets and maxima around the QWR perimeter where it joins the WL, favouring diffusion of arsenic atoms from these edges towards the QWR top (to increase its height) and outside (for the nucleation of new wires). Compositional profiles measured on the wetting

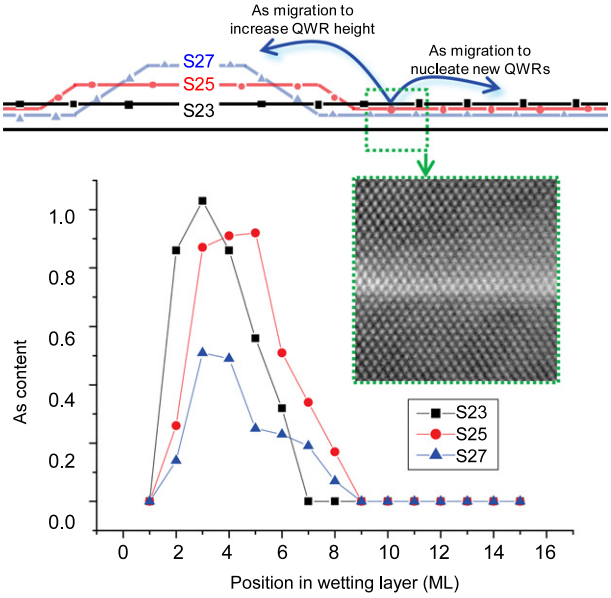

Figure 6. Arsenic content profiles of buried wetting layers in samples S23, S25 and S27, determined from high resolution aberration-corrected HAADF images, with an estimated error of ±0.18. In the case of S27 the image corresponds to an area in between two nearby QWRs. The inset is one of the HAADF images used for this analysis. Schematic morphological evolution and preferential As migration paths are represented at the upper side.

layers show its shrinkage in the regions around the wires as growth proceeds due to the migration of arsenic to lower energy areas. This gives additional support for the proposed growth reconstruction.

Acknowledgments

This work was supported by the Spanish MCI (TEC2008-06756-C03-02 and 03, Consolider-Ingenio 2010 IMAGINE CSD2009-00013 and QOIT CSD2006-0019), the Junta de Andalucia (PAI research groups TEP-120 and TIC-145; project P08-TEP-03516), the CAM (Q&CLight S2009ESP-1503) and the Office of Basic Energy Sciences, Division of Materials Sciences and Engineering, US DOE (MV and SJP).

References

[1] Stranski I N and Krastanow L 1937 *Sitz.ber. Akad. Wiss. Wien, Math.-Naturwiss. Klasse* **146** 797
[2] Seifert W, Carlsson N, Miller M, Pistol M E, Samuelson L and Wallenberg L R 1996 *Prog. Cryst. Growth Charact.* **33** 423–71
[3] González L, García J M, García R, Briones F and Martínez-Pastor J 2000 *Appl. Phys. Lett.* **76** 1104–6
[4] Fuster D, Gonzalez L, Gonzalez Y, Gonzalez M U and Martinez-Pastor J 2005 *J. Appl. Phys.* **98** 033502
[5] Molina S I, Ben T, Sales D L, Pizarro J, Galindo P, Varela M, Pennycook S J, Fuster D, González Y and González L 2006 *Nanotechnology* **17** 5652–8
[6] Molina S I, Varela M, Ben T, Sales D L, Pizarro J, Galindo P L, Fuster D, González Y, González L and Pennycook S J 2008 *J. Nanosci. Nanotechnol.* **8** 3422–6
[7] Fuster D, Alén B, González L, González Y, Martínez-Pastor J, González M U and García J M 2007 *Nanotechnology* **18** 035604
[8] Varela M, Lupini A R, van Benthem K, Borisevich A Y, Chisholm M F, Shibata N, Abe E and Pennycook S J 2005 *Annu. Rev. Mater. Res.* **35** 539–69
[9] Pennycook S J, Varela M, Lupini A R, Oxley M P and Chisholm M F 2009 *J. Electron Microsc.* **58** 87–97
[10] Pennycook S J *et al* 2009 *Phil. Trans. R. Soc.* a **367** 3709–33
[11] Molina S I, Varela M, Sales D L, Ben T, Pizarro J, Galindo P L, Fuster D, González Y, González L and Pennycook S J 2007 *Appl. Phys. Lett.* **91** 143112
[12] Bell G R, Kaijaks N S, Dixon R J and McConville C F 1998 *Surf. Sci.* **401** 125–37
[13] Molina S I, Sales D L, Galindo P L, Fuster D, González Y, Alén B, González L, Varela M and Pennycook S J 2009 *Ultramicroscopy* **109** 172–6
[14] Fuster D, Alén B, González L, González Y and Martínez-Pastor J 2007 *J. Cryst. Growth* **301/302** 705–8
[15] Gutiérrez H R, Cotta M A and De Carvalho M M G 2001 *Appl. Phys. Lett.* **79** 3854–6
[16] Levinstein M, Rumyantsev S and Shur M (ed) 1996 *Handbook Series on Semiconductor Parameters* vol 1 (London: World Scientific)
[17] Gatti R, Uhlík F and Montalenti F 2008 *New J. Phys.* **10** 083039
[18] Liu G R and Quek Jerry S S 2002 *Semicond. Sci. Technol.* **17** 630–3
[19] Liu P, Zhang Y W and Lu C 2003 *Phys. Rev.* B **68** 195314
[20] Biasiol G and Kapon E 1999 *J. Cryst. Growth* **201/202** 62–6
[21] Yang B, Liu F and Lagally M G 2004 *Phys. Rev. Lett.* **92** 025502
[22] Gutiérrez H R, Cotta M A, Bortoleto J R R and de Carvalho M M G 2002 *J. Appl. Phys.* **92** 7523–6
[23] Barabási A-L 1997 *Appl. Phys. Lett.* **70** 2565–7
[24] Leitsmann R and Bechstedt F 2008 *High Performance Computing in Science and Engineering '07* ed W E Nagel, D Kröner and M Resch (Leipzig: Elsevier) pp 107–16
[25] Claassens C H, Hoffman M J H, Terblans J J and Swart H C 2006 *J. Phys.: Conf. Ser.* **29** 185–9
[26] Kaganer V M and Ploog K H 2001 *Solid State Commun.* **117** 337–41
[27] Cho S O, Wang Zh M and Salamo G 2005 *J. Appl. Phys. Lett.* **86** 113106
[28] Muraki K, Fakatsu S and Shiraki Y 1992 *Appl. Phys. Lett.* **61** 557–9
[29] Tu Y H and Tersoff J 2007 *Phys. Rev. Lett.* **98** 096103
[30] Denker U, Rastelli A, Stoffel M, Tersoff J, Katsaros G, Costantini G, Kern K, Jin-Phillipp N Y, Jesson D E and Schmidt O G 2005 *Phys. Rev. Lett.* **94** 216103